Continental Shelf Research 173 (2019) 43–55

Contents lists available at ScienceDirect

Continental Shelf Research

journal homepage: www.elsevier.com/locate/csr

Observations of surface-gravity-wave scattering and dissipation by an isolated shoal related to a cuspate foreland

Juan F. Paniagua-Arroyave[a,b,c,*], Peter N. Adams[a], Sabrina M. Parra[d,e], Arnoldo Valle-Levinson[d]

[a] Department of Geological Sciences, University of Florida, Gainesville, FL, USA
[b] Área de Ciencias del Mar, Departamento de Ciencias de la Tierra, Universidad EAFIT, Medellín, Antioquia, Colombia
[c] Department of Earth, Ocean, and Atmospheric Science, Florida State University, Tallahassee, FL, USA
[d] Department of Civil and Coastal Engineering, University of Florida, Gainesville, FL, USA
[e] American Society for Engineering Education Postdoctoral Fellow at the Naval Research Laboratory, Stennis Space Center, MS, USA

ARTICLE INFO

Keywords:
Inner-shelf wave transformation
Wave refraction
Wave reflection
Wave diffraction
Infragravity waves
Cape-related shoals
Cape-associated shoals
Cape Canaveral shoals
Acoustic Doppler current profiler
Wave energy flux
Ursell number

ABSTRACT

Inner-shelf and shoreline morphology exert control on the variability of gravity waves. Although gravity waves can influence nearshore morphodynamics, their behavior is not well understood at inner-shelves close to cuspate forelands with complex bathymetry. In order to study the effects of cape shoals on gravity wave variability, water level and velocity data were collected during Fall 2013, Spring 2014, and Fall 2014 within the swales on either side of Shoal E, near Cape Canaveral, Florida. Short wave energy fluxes (periods from 3 to 20 s, or frequencies from 50 to ~300 mHz) were calculated from time series of spectral densities, whereas cross-shoal infragravity energy fluxes (periods from 20 to 500 s, or frequencies from 2 to 50 mHz) were calculated from cross-spectra of pressure and cross-shoal velocities. Ratios of short-gravity-wave energy fluxes between inner and outer swales of Shoal E ranged from 0.5 to 3. Values < 1 were typically associated to large (wave heights 1 m) and short waves (periods < 5 s) likely related to dissipation. Ratios 1 were exhibited by large and long (periods 10 s) waves because of refraction. Values close to 1 were related to small waves regardless of the wavelength. In addition, infragravity reflection coefficients were quantified as the ratio of seaward to landward infragravity energy fluxes. Reflection coefficients and spatial variations in infragravity fluxes indicate that instruments were located in the shoaling zone during Fall 2013 and Fall 2014. Infragravity energy flux differences between inner and outer swales further suggest Shoal E may have acted as a source of infragravity energy. Differences in reflection between swales on either side of Shoal E could be attributed to asymmetric short-wave shoaling and breaking, partial infragravity reflection, and infragravity energy trapping near the shoal. However, instrument configuration did not allow for along-shoal calculations, which hindered resolution of edge waves that might develop over the shoal. Our results provide evidence, albeit incomplete, of surface-gravity-wave energy scattering and dissipation over cape-related shoals. Such wave transformations, including infragravity energy forcing, may provide a positive feedback for the long-term stability of cuspate forelands by preventing the full complement of deep water wave energy from reaching the shoreline.

1. Introduction

Inner-shelf bathymetry influences the refraction, diffraction, and reflection (Bender and Dean, 2003) (collectively referred to as "scattering") and dissipation of surface gravity waves within the incident band. Nearshore processes and morphodynamics depend upon such wave transformations as they dictate the amount of energy available to transport pollutants, nutrients, organisms, and sediment (e.g., Rodriguez et al., 1995; Hoefel and Elgar, 2003; Schratzberger and Larcombe, 2014). For example, the long term evolution of sandy shorelines is determined by spatial gradients in long-shore sediment transport (Ashton and Murray, 2006; Kaergaard and Fredsoe, 2013, and others) and these gradients depend upon short-gravity wave transformation over site-specific bathymetry (e.g., Bender and Dean, 2003; Limber et al., 2017).

The short gravity waves (SGWs, frequencies f from 50 to ~300 mHz or periods from ~ 3–20 s) are typically modeled as rays of frequency-dispersive sinusoidal oscillations. Their wave heights increase, their

* Correspondence to: Juan Felipe Paniagua Arroyave, Departamento de Ciencias de la Tierra, Universidad EAFIT, Carrera 49 No. 7 Sur - 50, Oficina 19-613, Medellin, Antioquia, Colombia.
E-mail address: jpaniag2@eafit.edu.co (J.F. Paniagua-Arroyave).

https://doi.org/10.1016/j.csr.2018.12.004
Received 6 July 2018; Received in revised form 5 December 2018; Accepted 7 December 2018
Available online 08 December 2018
0278-4343/

celerities and wavelengths decrease during shoaling, and their wave rays deflect due to refraction by ambient currents and reductions in water depth (Mei et al., 2005, their Section 3.3). This behavior of wave rays determines the spatial distribution of wave energy and concurs with observations of energy divergence over submarine canyons and convergence at cuspate forelands (see e.g., Davidson-Arnott, 2010, Section 5.3.2 therein).

The frequency-dispersion assumption of wave ray modeling, however, does not hold near the shoreline. In the nearshore, frequency dispersion ($[\kappa h]^2$) diminishes while amplitude dispersion –nonlinearity (a/h)– increases, where κ is the wavenumber, h is the water depth, and a the waveform amplitude (Whitham, 1999, Section 13.11). This competition between frequency dispersion and nonlinearity can be represented by the Ursell number, given (in terms of wave statistics) by (Ursell, 1953; Doering and Bowen, 1986)

$$Ur = \alpha \frac{H_{SGW}}{h}\left(\frac{L}{h}\right)^2, \tag{1}$$

where $\alpha = (3\sqrt{2})/(64\pi^2)$, L is the wavelength, and H_{SGW} is the significant wave height for the SGW spectral band (Holthuijsen, 2007, Eq. 4.2.24 therein).

In deep water, $Ur \ll O(1)$ and frequency dispersion dominates over nonlinearity. Over complex bathymetry along some inner-shelves, weakly-nonlinear conditions prevail ($Ur \approx 1$) and the accurate modeling of nearshore morphodynamics requires the inclusion of nonlinear processes. These processes are typically well-identified in the surf zone for $Ur > 1$ (Young and Eldeberky, 1998) and include diffraction at caustics that might occur with shoals (e.g., Kirby and Dalrymple, 1983; Yoo and O'Connor, 1988), sea-swell breaking (e.g., Elgar and Guza, 1985; Filipot et al., 2010), and long gravity wave (LGW) generation and transformation (e.g., Elgar et al., 1992; Herbers et al., 1994).

Early studies found correlations between SGWs (sea-swell) and relatively longer oscillations that occurred in the low portion of the gravity (*infragravity*) band of frequencies (Munk, 1949; Tucker, 1950). Subsequent theoretical developments, as well as field and laboratory experiments have demonstrated the connection between these LGWs and the sediment transport in surf and swash zones (Aagaard and Greenwood, 2008; Alsina et al., 2016, and others) beach cusp formation via nearshore-trapped edge waves (e.g., Bowen and Guza, 1978; Coco et al., 2003), instabilities in longshore currents (Feddersen, 2014), wave-breaking (Clark et al., 2012), water level variations in harbors (Bowers, 1977; Diaz-Hernandez et al., 2015), and coastal erosion during storms (Guza and Thornton, 1982; Roelvink et al., 2009; Young et al., 2012). The reader is referred to Bertin et al. (2018) for a recent review on infragravity waves.

Considering only irrotational motions, nearshore LGWs typically result from the combination of free and forced waves (Okihiro et al., 1992; Rijnsdorp et al., 2015, and others). Forced LGWs (i.e., surf beats) are oscillations linked to frequency-dispersive, short-wave groups via difference interactions (Herbers et al., 1994; de Bakker et al., 2015). Within a group of dispersive SGWs exists a spatial variability in wave heights and, therefore, in period-averaged stresses related to wave orbital velocities (also known as wave radiation stresses).

For horizontal bottoms and wave groups that are long compared to the water depth, the spatial gradient in radiation stresses generates a spatially-varying wave set-down in phase with the wave group envelope, or “surf beat” (analogous to the sound beat) that travels with the group but has a mass transport opposed to the group's propagation (Longuet-Higgins and Stewart, 1964). In addition, on sloping bottoms the difference in water depth within the group induces a spatially-variable forced wave and a dynamic set-up, i.e., free LGWs that propagate both in the direction of wave groups, and the opposite direction (Baldock, 2006). Forced infragravity waves are typically small in deep water with amplitudes $O(10^{-3}\,\mathrm{m})$, but can be larger in the surf and swash zones with amplitudes ranging from $O(10^{-1}\,\mathrm{m})$ *to* $O(1\,m)$ (e.g., Ruessink, 1998).

Bathymetry exerts control on forced infragravity motions via variations in water depth, bottom slope, and bottom curvature. These geometrical features influence the level of energy transfer between the sea-swell and the LGW frequencies (e.g., Janssen et al., 2006, their Eq. A1). Energy transfers have been extensively studied during recent decades (Hasselmann, 1962; Elgar et al., 1993; Herbers et al., 2000b; de Bakker et al., 2016, and others), and have been found to depend on the character of bottom sedimentary material (Torres-Freyermuth and Hsu, 2014) and overall profile shape (Thomson et al., 2006; de Bakker et al., 2016, and others).

In addition to forced motions, free LGWs that obey the shallow water dispersion relationship, $[\omega/\kappa]^2 = gh$ (where ω is the radian frequency and g is the acceleration due to gravity) have been found to be either locally- or remotely-generated. Remote sources refer to shoreline reflections across the ocean (Herbers et al., 1995). Local sources include reflections from nearby shorelines, the dynamic set up produced by the shoaling of wave groups (Liu, 1989; Zou, 2011), and the time-varying breaking of short waves within groups (Symonds et al., 1982; Schäffer, 1993).

Bottom morphology influences free LGWs variability via partial reflections, trapping, and short-wave breaking. Passive-margin, wide continental shelves can trap free LGWs (Herbers et al., 1995), whereas submarine canyons can partially-reflect incoming infragravity waves (Thomson et al., 2007), and short-wave breaking dominates LGW variability on fringing reef lagoons (Pomeroy et al., 2012). However, at locations characterized by complicated inner-shelf bathymetry adjacent to high-curvature shorelines, like cape-related shoals near cuspate forelands, the variability of LGWs has not been explored. The presence of capes and associated shoals at settings of relatively high socio-economic importance highlight the need for understanding in situ gravity wave behavior, which likely influences the long-term evolution of adjacent shorelines (McNinch and Luettich, 2000; Thompson et al., 2015; Murray and Ashton, 2013, and references therein).

In this manuscript we combine field observations with wave theory to analyze the effect of cape-related shoals on gravity wave variability. We hypothesize that wave characteristics dictate the amount of energy flux available in the lee of isolated, cape-related shoals. In Section 2 we describe the methodology including the study area, as well as data collection and analysis. Section 3 describes the ratio of SGW energy fluxes and infragravity reflection coefficients between swales, and compares energy fluxes measured at inner and outer swales on either side of a cape-related shoal. In Section 4 we discuss our results in light of short-wave scattering and dissipation. Our results suggest that an isolated shoal close to a cuspate foreland dissipated large SGWs regardless of the wavelength and refracted only the longest and largest SGWs. They also suggest that the isolated shoal generated seaward SGWs and dissipated landward LGWs, with a net gain in energy fluxes in the lee of the shoal. Competition of refraction and dissipation as a function of wave characteristics could explain differences in SGW energy fluxes. Similarly, sea-swell asymmetric shoaling and de-shoaling may explain differences in LGW energy fluxes. Conclusions are provided in Section 5.

2. Data and methods

2.1. Study area

Canaveral shoals occupy depths between 5 and 25 m along the inner shelf, adjacent to Cape Canaveral, on the Atlantic coast of Florida. The shore-attached Southeast shoal is an offshore extension of Cape Canaveral (Fig. 1). The isolated shoal of interest –Shoal E– is located ~ 3 km from Southeast shoal, from which it is separated by a shallow basin that is ~ 15 *m* deep (Field and Duane, 1974; Thompson et al., 2015). Its approximate orientation, taken as ~ 22 °T (with °T as the azimuth, or ° East of North), was used to calculate azimuth ranges that define the cross-shoal wave propagation D_p, which is the short-wave peak direction in the

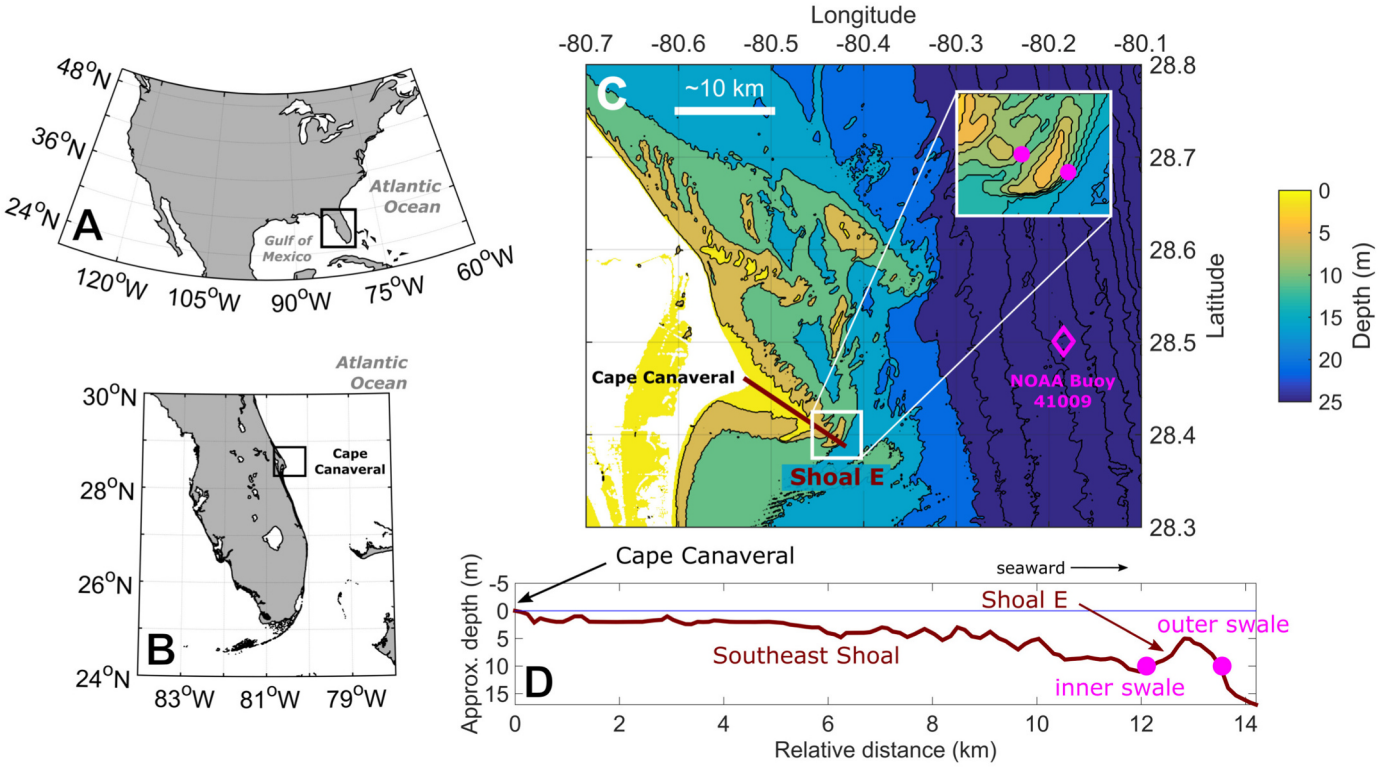

Fig. 1. Location of acoustic Doppler current profilers (ADCPs) at Cape Canaveral shoals. Magenta filled circles represent the approximate ADCP locations at the outer and inner swales of Shoal E (water depths ~ 13 m). Black rectangles in A and B show the location of the Florida Peninsula within North America and Cape Canaveral on the Florida Peninsula, respectively. The map in C shows the inner shelf bathymetry near Cape Canaveral with an inset highlighting Shoal E. Contours indicate water depths in intervals of 5 m. The brown line corresponds to an approximate bottom profile across Southeast shoal and Shoal E (D). Bathymetric data available at the NOAA Geophysical Data Repository. The package M_Map was used to create North America and Florida maps (https://www.eoas.ubc.ca/rich/map.html). (For interpretation of the references to colour in this figure legend, the reader is referred to the web version of this article.)

meteorological convention as defined by Benoit et al. (1997): $D_p \in (67°\text{T}, 157°\text{T})$ is landward, and $D_p \in (247°\text{T}, 337°\text{T})$ is seaward.

Previous studies in this region (Olsen Associates, 2013) and similar locations (McNinch and Luettich, 2000; Thieler et al., 2014) found that shoals can migrate at rates $O(10\ m\ yr^{-1})$ and might experience active reworking by oceanographic processes, such as the rectification of tidal and subtidal flows (Signell and Geyer, 1990; Geyer, 1993; Berthot and Pattiaratchi, 2005; Lamas et al., 2017), wind-related flows, and surface gravity waves (McNinch and Luettich, 2000; Kumar et al., 2013). Canaveral shoals, in this regard, are thought to be a nearshore sediment sink. This idea is supported by the presence of ooids (spherical grains composed of calcium carbonate) in the shoals and adjacent shorelines, suggesting a sedimentary connection between beaches and shoals (Field and Duane, 1974).

Water levels are dominated by semi-diurnal (M_2 and N_2), and diurnal (K_1 and O_1) tidal constituents. Spring tidal ranges are ~ 1.5 m and neap ranges are ~ 0.4 m. As shown by the buoy 41009 from the National Oceanic and Atmospheric Administration (NOAA), the wave climate exhibits seasonal variability (Fig. 2). During summer months (June to August) the offshore wave field is mildly energetic ($H_s \approx 0.5m$, Fig. 2A, C, and E; $T_p \approx 8\ s$, Fig. 2B, D, and F) propagating from the east ($D_p \approx 90\ °T$), while during winter and spring (October to April) Nor'easter activity tends to dominate ($H_s > 2m$, $T_p > 10s$) with waves coming from the north-northeast ($D_p < 60°T$ and $D_p > 330°T$) (Kline, 2013, Fig. 2 herein). In this case, each H_s value corresponds to the mean value of the highest one-third of all wave heights measured during the first 20 min of every hour and should not be confused with the SGW significant height, H_{SGW}, which is used later in this manuscript. Seasonality in wave climate also includes tropical cyclone activity during summer and early fall (June through November). During hurricanes, wave conditions at shoals can reach values $H_s > 6\ m$, $T_p \approx 10\ s$, and . Infragravity frequencies ranged from 5 to 50 mHz (or 20–200 s), comparable to other locations along the US Atlantic Coast (Herbers et al., 1994), and LGWs significant wave heights ranged from 0.02 to 0.2 m.

2.2. Data collection and processing

Observations of water velocity and near-bottom pressure were obtained from upward-looking acoustic Doppler current profilers (ADCPs) at the inner and outer swales on either side of Shoal E (Fig. 1 C and D). Field experiments were conducted during Fall 2013 (September 23rd to December 3rd), Spring 2014 (May 6th to June 6th), and Fall 2014 (October 8th to January 7th of 2015). Pressure and velocity data were recorded in bursts of 1200, 2048, 2400, or 3600 measurements at a sampling frequency of $2\ Hz$. Pressure was measured ~ 1 m above the bed and corrected for attenuation with depth (Bishop and Donelan, 1987; Raubenheimer et al., 1998), while wave orbital velocities were obtained at a single depth ~ $7\ m$ above the bed (see Paniagua-Arroyave et al., 2018 for details in experimental set-up).

Data processing included the screening for anomalous measurements in time when instruments were not submerged, when spikes occurred, or when there were low correlations among velocities measured by different transducers (Goring and Nikora, 2002; RDI, 2011). Given the water depths and wave properties (typically $Ur < 0.1$), observed deviations from linear wave theory were considered negligible (Elgar et al., 2005). To quantify SGW characteristics and analyze the LGW energy variability, power spectra, $\mathcal{S}(f)$, with frequency resolutions, df, of 4 mHz (hereafter referred to as "low resolution") and 1 mHz ("high resolution") were calculated for pressure burst data packets that were de-meaned and de-trended. Because sampling

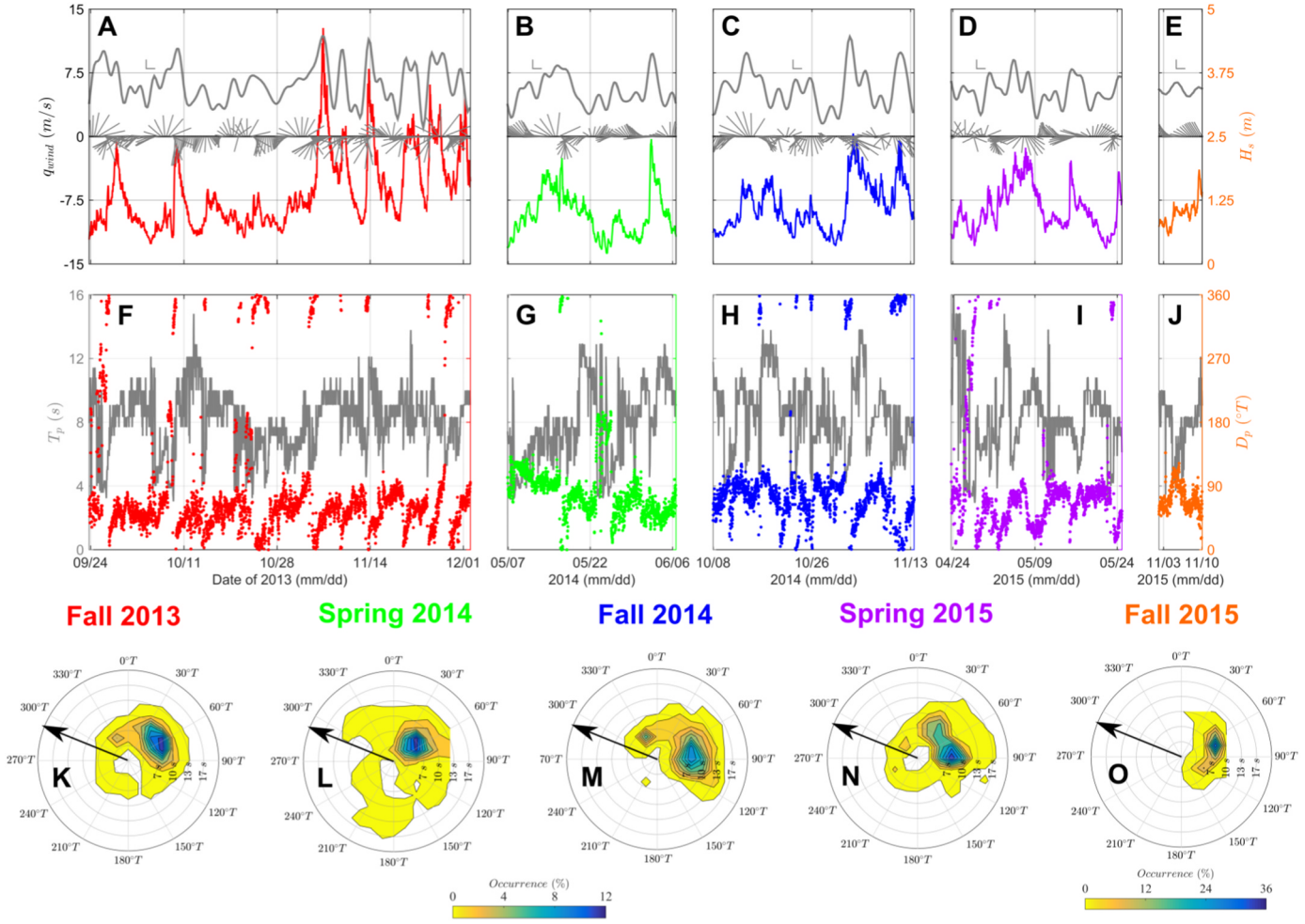

Fig. 2. (A–F) Time series of wave conditions at the NOAA 41009 buoy (location 28.501 N, 80.184 W) offshore of Cape Canaveral, Florida Atlantic coast, during deployments at Canaveral shoals. (A, C, and E) Colored lines represent significant wave heights, H_s in m, gray lines represent wind speed, q_{wind} in m/s, and gray sticks point to direction from which the wind blew (meteorological convention). (B, D, and F) Colored dots show the peak direction, D_p (in azimuth degrees, °T), and gray lines represent the peak period, T_p (in s). (G through I) Joint histograms of peak period, T_p (in s), and peak direction, D_p (in °T), for NOAA buoy 41009 data during each deployment. Contours represent the percentage of occurrence for a combination of period and direction according to the colorbar at the bottom. Black arrows indicate the approximate onshore direction perpendicular to Shoal E axis. Buoy #41009 data made available by the National Data Buoy Center (NDBC) at http://www.ndbc.noaa.gov/station_page.php?station=41009/. (For interpretation of the references to colour in this figure legend, the reader is referred to the web version of this article.)

Table 1
Parameters of spectral calculations for each experiment. DOFs: degrees of freedom (Thomson and Emery, 2014, their Section 5.4.6).

Experiment	Swale	Number of measurements		DOFs	
		Burst	3-h package	Low res.	High res.
Fall 2013	Inner	1,200[a]	3,600	36	20
	Outer	2,048[b]	12,288	180	84
Spring 2014	Inner	2,400[a]	7,200	100	36
	Outer	2,400[a]	7,200	100	36
Fall 2014	Inner	N/A[c]	21,600	324	148
	Outer	2,400[a]	7,200	100	36

[a] One burst at 2 Hz measured every hour.
[b] Burst at 2 Hz measured every 32 min.
[c] Data continuously measured at 2 Hz.

frequencies were instrument specific, we assembled bursts into 3-h ensembles and assumed stationarity over each of those intervals. To reduce the effects of Gibbs phenomenon, we tapered (with a Hann function) and 75%-overlapped data windows of $2^{10} = 1024$ and $2^{11} = 2048$ elements to calculate the low and high resolution spectra, respectively (Thomson and Emery, 2014, their Section 5.4.6). See Table 1 for details about the spectral calculation.

2.3. Wave properties and short gravity wave energy fluxes

Using time series of spectral density values, $\mathcal{S}(t, f)$, SGW significant wave heights, $H_{SGW}(t)$, were calculated for each deployment as $H_{SGW}(t) \approx 4\sqrt{m_{SGW}(t)}$ (Holthuijsen, 2007, Eq. 4.2.24 therein), where $m_{SGW}(t) = \int_{50\ mHz}^{300\ mHz} S(f, t)df$ is the zeroth-moment of the sea surface variance spectrum for the short gravity band (frequencies between 50 and 300 mHz, periods from ~ 3 to 20 s) (Thomson and Emery, 2014, their Eq. 5.121 and Section 5.6.3). Wave properties also include peak periods, T_p in seconds, and peak direction, D_p in azimuth degrees (starting from zero at North and increasing to 360 °T clockwise). The former was calculated as the inverse of the frequency at which the maximum value of spectral density was found for each spectrum, whereas the latter corresponded to the direction that coincided with the maximum spectral value in each directional spectrum (Benoit et al., 1997).

Using wave properties, we calculated, for each spectrum, the SGW energy flux for long-crested waves (or the energy transport per unit

time per unit crest length, or wave power), P in units of W/m as (Holthuijsen, 2007, Eq. 5.5.12 therein)

$$P = Ec_g, \tag{2}$$

with $E = g\rho a^2/2 = g\rho H_{SGW}^2/16$ (Lentz and Fewings, 2012), $c_g = cn$ as the group velocity, $c = \omega_p/k$ as the phase velocity, $n = 0.5(1 + 2\kappa h/\sinh(2\kappa h))$, and $\omega_p = 2\pi/T_p$. Recall that it is assumed that $\omega_p^2 = gk\tanh(kh)$ (Guo, 2002). In order to assess the effect of shoal bathymetry on wave scattering and dissipation, we quantified the ratio of wave power between swales, P_{ratio}, as

$$P_{ratio} = \frac{P_{inner}}{P_{outer}}, \tag{3}$$

with P_{inner} and P_{outer} representing the wave power at the inner and outer swales, respectively. Values of 1 indicate no transformation between swales, whereas values >1 indicate a seaward increase in energy flux (from inner swale to outer swale). We then analyze P_{ratio} in a five-dimensional space formed by P_{ratio}, Ur, D_p, T_p, and κh to discern the variability of energy flux between swales under different conditions of nonlinearity, direction of approach, sea or swell sources, and deep-intermediate-shallow water character.

2.4. Long gravity energy fluxes

Assuming cross-shoal propagation only, seaward and landward cross-shoal LGW energy fluxes were estimated from time series of pressure, P, and velocity, $\vec{q} = (u, v)$, where u and v are the East-West and North-South orbital velocity components, respectively. Cross- and along-shoal velocities were calculated as the projections of $\vec{q}$ to a coordinate system aligned with the angle of the shoal axes, i.e. ~ 22 °T. As such, velocities in the shoal coordinate system were defined as $\vec{Q} = (U, V)$, with U and V being the along- and cross-shoal velocities, respectively. Without including water density as it was proposed in the literature, the LGW energy fluxes $\mathcal{F}^{\pm}(f)$ at each location (with "+" being landward and "−" seaward) were calculated from the momentum balance of shallow water waves as (Sheremet et al. 2002)

$$\mathcal{F}^{\pm}(f) = \frac{\sqrt{gh}}{4}\left[Co_{PP}(f) + \frac{h}{g}Co_{VV}(f) \pm 2\sqrt{\frac{h}{g}}Co_{PV}(f)\right], \tag{4}$$

where Co_{xy} represents the coincident spectrum –the real part of the cross-spectrum– between time series x and y, e.g. Co_{PV} is the coincident spectrum between time series of pressure, P, and cross-shoal velocity, V (e.g., Thomson and Emery, 2014, their Section 5.6.5). Bulk energy fluxes $F^{\pm}$ were then quantified as the integral sum of $\mathcal{F}^{\pm}(f)$ within the long gravity band (0.5–50 mHz). From seaward- and landward-oriented LGW energy fluxes, the cross-shoal reflection coefficient, R^2, was calculated as

$$R^2 = \frac{F^-}{F^+}. \tag{5}$$

This symbology for the reflection coefficient, R^2, is chosen to be consistent with Sheremet et al. (2002), and should not be confused with the coefficient of determination, r^2.

3. Results

3.1. Spectrograms and gravity wave variability

Fig. 3 shows spectrograms (the time series of low resolution spectra) and significant wave heights for the short gravity band, H_{SGW}, for each of the three experiments. The time series of spectral density values represent the variance at different times and frequencies. Most of this variance, i.e. relatively larger oscillations, was measured at frequencies between 50 and 300 mHz, or ~ 3–20 s. When waves were relatively large within this band, approximately corresponding to when H_{SGW} > 1.5 m, oscillations were correspondingly more prominent at frequencies below 50 mHz (cf. Fig. 3A and B around dates 11/5 and 11/14 of 2013).

The opposite was also found: during events when $H_{SGW} < 0.3m$, variances within the LGW band (around 10 mHz) were approximately 10^{-4}m^2/Hz (see Fig. 3C and D at 5/25, or E and F at 10/30). Moreover, during instances when oscillations were negligible at frequencies ~ 10 mHz, LGW variance at 3 mHz was relatively high (e.g. 3C at 5/22). These observations suggest the partition of forced and free LGWs found elsewhere (e.g., Herbers et al., 1994, 1995).

To analyze the dependence of LGWs on SGWs and obtain an approximate distribution of forced and free LGWs, we calculated the coefficients of determination, $r^2_{LGW,SGW}$, between the time series of spectral densities at each frequency within the LGW band, and the SGW (sea-swell) variance, $m_{0,SGW}$ (Okihiro and Guza, 1995). Overall, ~ 50% of the variance at LGWs frequencies between ~ 5 mHz (200 s) and 50 mHz (20 s) was explained by the variability of $m_{0,SGW}$ at the 95% confidence level (Fig. 4 A for the inner swale, and B for the outer swale). At frequencies lower than ~ 5 mHz (periods higher than 200 s), ~ 1 to ~ 15% of LGW variance variability was explained by variations in $m_{0,SGW}$. During Fall 2013 at the outer swale, H_{SGW} explained nearly 75% of LGW variability (red line in Fig. 4B), in contrast to ~ 60% explained at the inner swale (Fig. 4 A). That tendency was reversed during Spring 2014 (~ 50% at outer versus ~ 60% at inner) and Fall 2014 (40–50% at outer versus 50–60% at inner). Differences in LGW-SGW correlations between swales could be representative of the decrease in forced LGWs at the "outer" swale (in the lee of Shoal E) after short-wave propagation.

Figs. 4C and D illustrate the mean spectra (from "high resolution" spectra), $\overline{\mathcal{S}}(f)$, for each deployment. The mean spectra were computed by time-averaging the spectral densities at each frequency for all high-resolution spectra (cf. Fig. 3). The infragravity band was defined between 1 and 50 mHz (or 20–1000 s) by the drop in mean spectral density in the sea-swell band, defined between 50 and 300 mHz, or 3–20 s (cf. all panels in Fig. 3, and Figs. 4C, inner swale, and 4D, outer swale). This frequency band separation agrees with other studies conducted along the U.S. North Atlantic coast (e.g., Herbers et al., 1994).

3.2. Short wave energy flux variability between swales

We compared the ratio of SGW energy fluxes between swales as a function of SGW properties at the outer swale: ratio of frequency-amplitude dispersion (Ur), peak direction (D_p), peak period (T_p), significant wave height (H_{SGW}), and frequency dispersion (κh). This comparison tests the hypothesis that wave properties dictate the amount of energy flux available in the lee of isolated, cape-related shoals. Fig. 5 shows the compilation of P_{ratio} values for two arbitrarily chosen categories of SGWs based on wave properties: short ($Ur < 4 \times 10^{-3}$, $T_p < 5\,s$, and $\kappa h \approx 0$) and long ($Ur > 4 \times 10^{-3}$, $T_p > 10\,s$, and $\kappa h \approx \pi$). The occurrence of short and long SGWs did not depend on peak direction (Fig. 5A).

For the short SGW category (Fig. 5B and C), values of P_{ratio} were typically less than 1.1, with H_{SGW} increasing as P_{ratio} decreased, except for the observation of $Ur \approx 6 \times 10^{-4}$, $P_{ratio} \approx 0.5$ and $D_p \approx 270°T$ (Fig. 5B). Values of P_{ratio} for the long SGW category, in contrast, ranged between 0.7 and 3. Values of H_{SGW} tended to increase with Ur for this category, with values of $H_{SGW} > 1$ m associated with energy flux ratios between 0.7 and 1.5. The extreme P_{ratio} values were related to relatively small, relatively long waves that traveled from the East ($H_{SGW} \approx 0.5\,m$, $T_p > 10\,s$, and $D_p \approx 90°T$). Most of the short and long SGWs (≈ 30%) traveled from directions between 45 and 90°T (Fig. 5D).

Values of P_{ratio} and wave properties for intermediate SGWs ($2 \times 10^{-3} < Ur < 8 \times 10^{-2}$, $5\,s \le T_p \le 10\,s$, and $0.5 < \kappa h < 2.5$) are shown in Fig. 6. These observations overlap with short and long SGWs observations and occur without a dependence on D_p, as well (Fig. 6A). Relatively small ($H_{SGW} \approx 0.5\,m$), and short ($Ur \approx 2 \times 10^{-3}$ and $\kappa h \approx 2.5$) SGWs in this category were associated with values of $0.5 < P_{ratio} < 1.2$ (Fig. 6B). Values of P_{ratio} ranged between 0.5 and 2.1

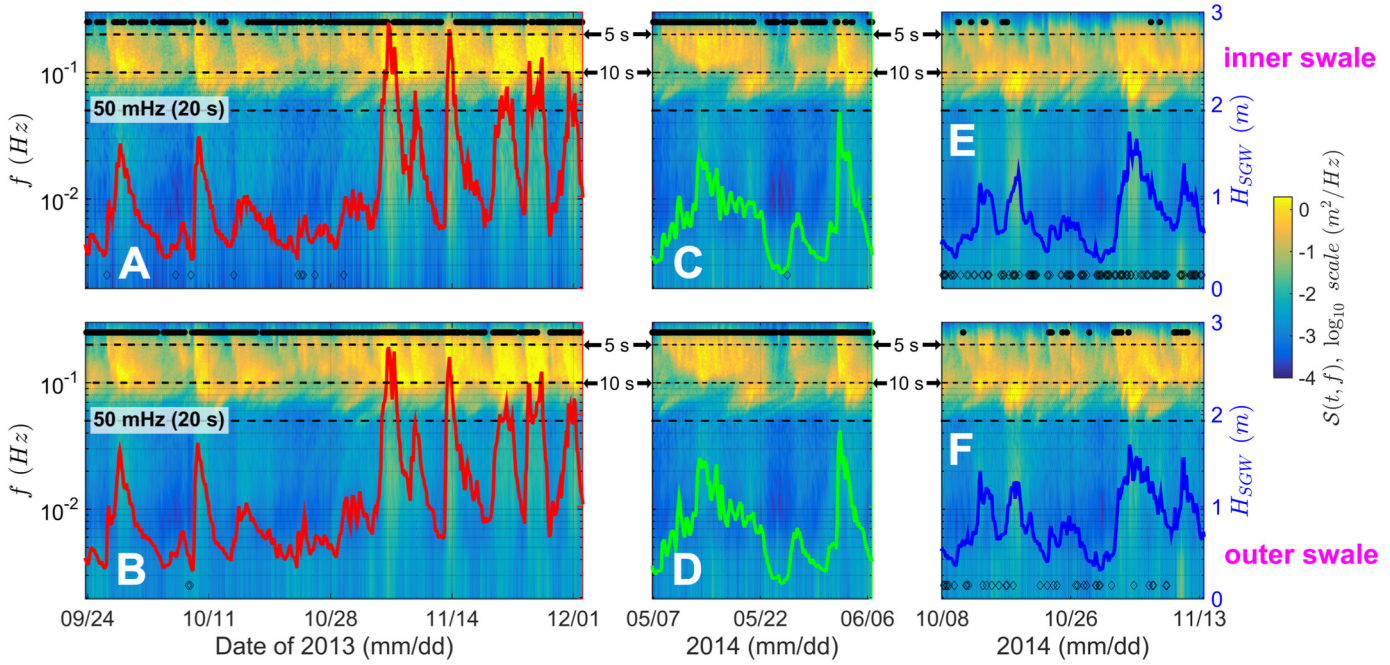

Fig. 3. (A–F) Spectrograms, $\mathcal{S}(t, f)$, show unsteady variance at the long gravity (*infragravity*) band (frequencies below 50 mHz, or above 20 s). Upper panels correspond to measurements at the inner swale, whereas lower panels to the outer swale. Experiments were conducted during Fall 2013 (A and B), Spring 2014 (C and D), and Fall 2014 (E and F). Each "low resolution" spectrum was calculated from detrended, Hanning-windowed, 75% overlapped, and attenuation-corrected pressure values measured during 3-h intervals. Red, green, and blue lines correspond to SGW significant heights, H_{SGW}, for Fall 2013, Spring 2014, and Fall 2014, respectively. Degrees of freedom for each 3-h spectrum are (A) 36, (B) 180, (C, D, and F) 100, and (E) 324. Top filled circles and bottom hollow diamonds represent instances at which waves propagated within a 45° window of perpendicularity to Shoal E in the landward and seaward directions, respectively. (For interpretation of the references to colour in this figure legend, the reader is referred to the web version of this article.)

for $0°T < D_p < 180°T$, and between 0.5 and 1.5 for $180\ °T < D_p < 360°T$ (Fig. 6C). Similarly to short and long SGWs, waves mostly approached from directions between 45 and 90 °T.

Our observations suggest that large SGWs propagation (either short or long) was influenced by dissipation (including bottom friction by ripples), whereas for long and large SGWs the effect of refraction by Shoal E surpassed dissipation. In other words, the largest P_{ratio} values were found for large and long SGWs (dissipation and refraction as expected from linear wave theory), whereas smallest values of P_{ratio} were found for large and short SGWs (only dissipation). In summary we observed:

1. Short SGWs ($Ur < 4 \times 10^{-3}$, $T_p < 5\,s$, and $\kappa h \approx 0$) were associated with $P_{ratio} < 1.\ 1$, with P_{ratio} values decreasing as H_{SGW} increased.
2. Long SGWs ($Ur > 4 \times 10^{-3}$, $T_p > 10\,s$, and $\kappa h \approx \pi$) were related to $0.7 < P_{ratio} < 3$, with $H_{SGW} > 1\,m$ for $P_{ratio} < 1.\ 5$.
3. Intermediate SGWs ($2 \times 10^{-3} < Ur < 8 \times 10^{-2}$, $5\,s \leq T_p \leq 10\,s$, and $0.5 < \kappa h < 2.\ 5$) overlapped with short and long SGWs observations.

3.3. Infragravity energy fluxes between swales

In addition to the hypothesis of shoal control on SGWs via refraction and dissipation, we also hypothesize that cape-related shoals exert control on the spatial transformation of infragravity waves. To test this, we compare cross-shoal seaward (F^-) and landward (F^+) LGW energy fluxes at inner and outer swales of Shoal E (Fig. 7). Three spatial structures were identified: In comparison to outer swale fluxes, we observed larger fluxes at the inner swale during Fall 2013 (Fig. 7A and B), nearly comparable fluxes at the inner swale during Spring 2014 (Fig. 7C and D), and smaller fluxes at the inner swale during Fall 2014 (Fig. 7E and F). Differences in fluxes suggest that the source (or sink) of LGW energy between the swales may be related to short-wave shoaling and breaking over the shoal.

In addition, we quantified the cross-shoal bulk LGW reflection coefficients (R^2) at inner and outer swales of Shoal E. These reflection coefficients represent the fraction of seaward (outgoing) infragravity energy flux relative to the landward (incoming) infragravity energy flux, i.e. the level of reflection of infragravity waves. Ranges of R^2 values are associated with regimes governing the infragravity wave field: the inter comparison between dissipation and local generation (Sheremet et al., 2002).

Table 2 summarizes the results from an inference analysis (Devore and Berk, 2012, their Eq. 10.1) performed on reflection coefficients between swales. On average, mean reflection coefficients at the outer swale were not equal to those at the inner swale at the 99% confidence level (Bendat and Piersol, 2010, their Eq. 4.61). Furthermore, R^2 values were typically larger at the outer swale during all experiments.

To analyze the level of reflection and quantity of infragravity energy with respect to the short-wave behavior, R^2 values (Fig. 8 A, C, and E) and LGW heights (Fig. 8B, D, and F) were assessed as functions of the Ursell parameter, and sorted by peak direction, D_p, and peak period, T_p. We recognize two consistent tendencies:

1. $R^2 \approx 1$ for $Ur \in (5 \times 10^{-4}, 5 \times 10^{-3})$ and $T_p < 8\ s$.
2. $R^2 \in (0.4, 3)$ when $T_p > 10\ s$.

The relative angle of wave propagation with respect to the shoal axis showed two additional tendencies:

1. $R^2 < 1$ when $D_p \in (67°, 157°)$, i.e. landward propagation across the shoal
2. $R^2 > 1$ when $D_p \in (247°, 337)°$, i.e. seaward-directed waves.

Opposite tendencies in R^2 values between Fall seasons of 2013 and 2014 for Ur larger than 2×10^{-2} (cf. Figs. 8A and E) may be explained as an artifact of $F^{\pm}$ positive direction being arbitrary. This sign choice depends upon the cross-shoal velocity (V) direction. In that vein, F^- and F^+ correspond to seaward and landward propagations,

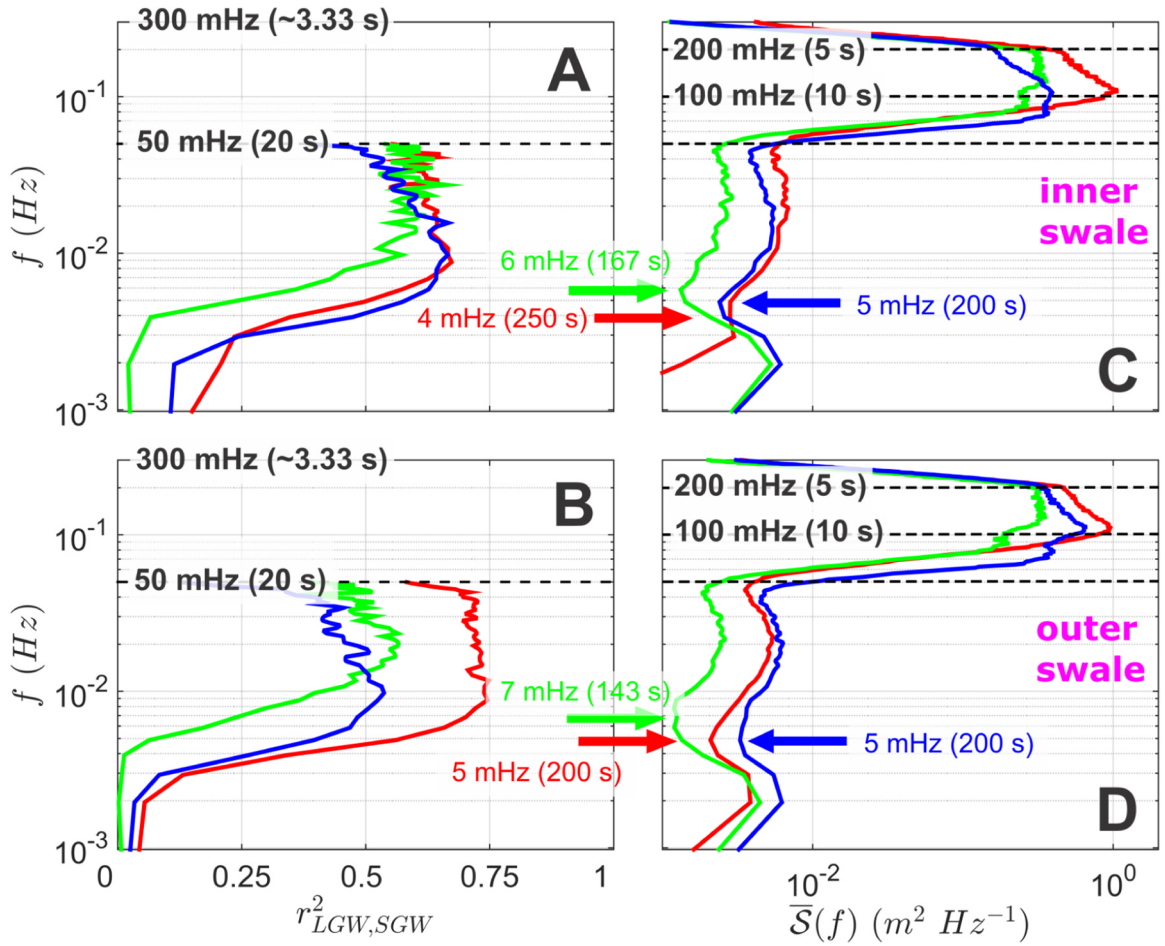

Fig. 4. (A and B) Coefficients of determination (significant at the 95% level of statistical confidence) between H_{SGW} and time series of infragravity spectral densities at each frequency, $r^2_{LGW,SGW}$. Red, green, and blue lines represent Fall 2013, Spring 2014, and Fall 2014 deployments, respectively. A and C correspond to the inner swale observations, whereas B and D correspond to the outer swale. (C and D) Mean spectra, $\overline{S}(f)$, with two LGW sub-bands as shown by drops in mean spectral density at ~ 50 *mHz* and 4 to 6 *mHz* (color arrows), which correspond to the two groups with different correlations with H_{SGW}, and three sub-bands for the SGW portion of the spectrum according to Fig. 3: 20–10 s, 10–5 s, and less than 5 s. (For interpretation of the references to colour in this figure legend, the reader is referred to the web version of this article.)

respectively, which are linked to the sign in the last term of Eq. (4). During Fall 2014 when waves with *Ur* larger than 5×10^{-2} have directions between 247° and 337° (i.e., seaward across the shoal), values of R^2 were typically larger than 1. These R^2 values suggest that seaward fluxes were greater than landward fluxes ($F^- > F^+$) and waves behaved as in deep water (Sheremet et al., 2002).

However, if the incoming and outgoing roles are exchanged, with respect to the short-wave direction of propagation, i.e. F^+ represents seaward fluxes when waves propagate seaward across the shoal, then $F^{\pm}$ directions are reversed and R^2 values suggest a different regime. For *Ur* larger than 5×10^{-2}, Fall 2014 values of R^2 would be less than 1 and would suggest the shoal to be located in the shoaling zone as in during Fall 2013. In synthesis, R^2 values suggest that LGW energy fluxes that oppose the short-wave propagation direction were smaller than fluxes in the direction of the sea-swell when *Ur* was larger than $\sim 5 \times 10^{-2}$.

4. Discussion

We hypothesized that wave characteristics dictate the amount of energy flux available in the lee of isolated, cape-related shoals. In other words, shoals affect SGWs and LGWs via refraction, diffraction, reflection, dissipation, and trapping. Differences in SGW energy fluxes between swales and higher long gravity wave R^2 values at the lee (swale) of Shoal E suggest that the refraction and dissipation of waves is dependent upon wave characteristics and the behavior of Shoal E as a source (sink) of seaward (landward) cross-shoal LGW energy flux. Seasonality may play a role in gravity wave variability since LGW observations during both Fall experiments followed similar trends and differed from Spring results.

4.1. Shoaling and breaking of short-gravity-waves linked to infragravity energy variability

We discuss shoaling and breaking of wave groups as the first mechanism that may operate over Shoal E with regard to LGWs. Long-gravity waves can be generated over shoals by spatial differences in water depth along wave groups that amplify their wave set-up (Mei and Benmoussa, 1984; Baldock, 2006). Infragravity waves can also be generated by the time-varying short-wave breaking within groups (Schäffer, 1993), and via enhanced energy transfer from sea-swell (Beji and Battjes, 1993).

The relationship between R^2 and *Ur* (Fig. 8A and E) resembles the dependence of the phase among interacting wave triads (phase of the bispectrum), wave asymmetry, and wave skewness on *Ur* (Doering and Bowen, 1995, their Fig. 7). This dependence suggests that R^2 values $O(10^{-1})$ were related to weakly-nonlinear waves (Young and Eldeberky, 1998). Parameterizations of the skewness, S_{ww}; asymmetry, A_{ww}; and biphase, β_{ww}, are given in terms of *Ur* as (Doering and Bowen, 1995, their Eqs. 4.9-4.11)

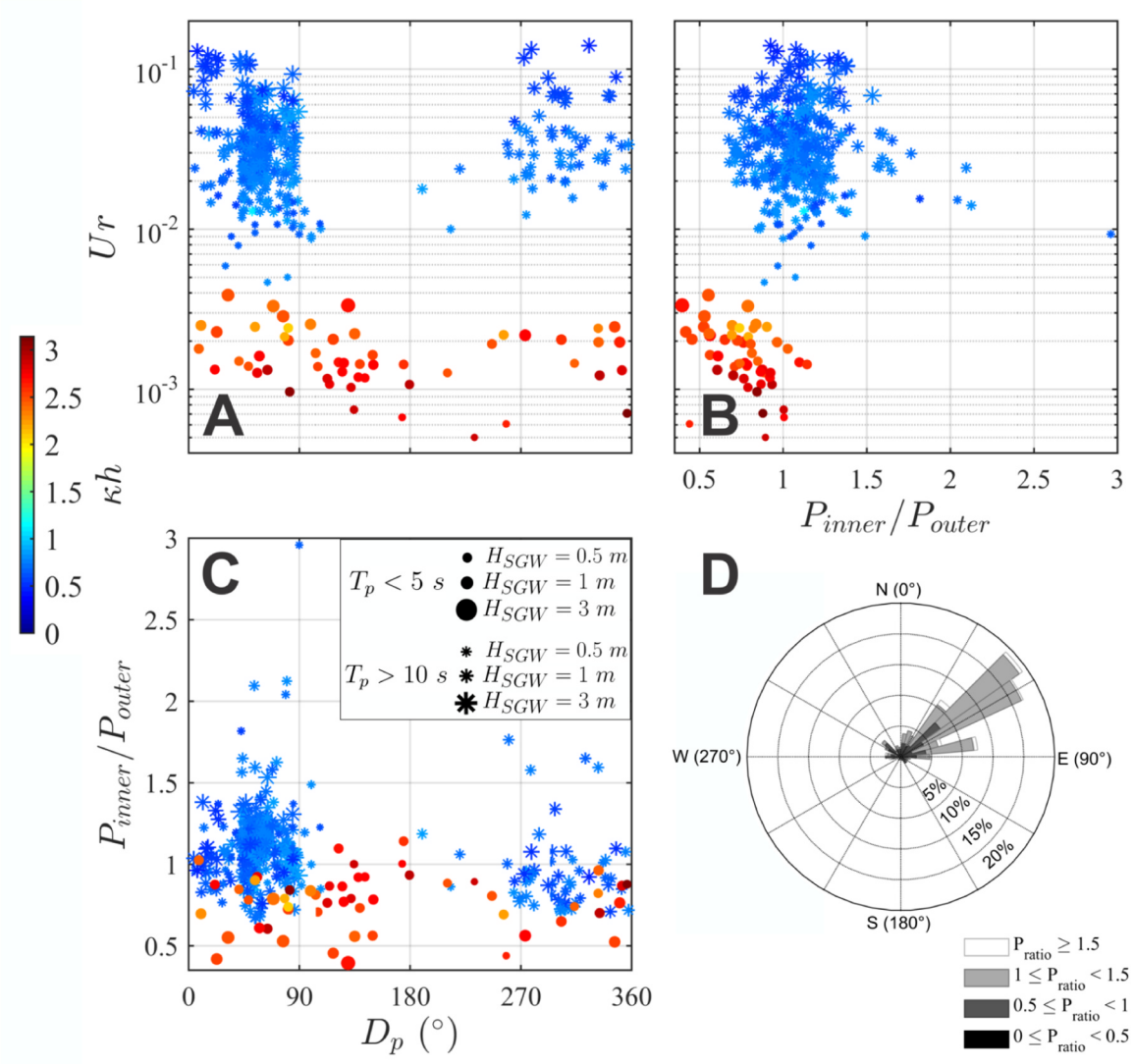

Fig. 5. Ratio of short and long SGW energy fluxes between swales as a function of short wave properties at the outer swale. (A) Ursell number, Ur, versus peak direction, D_p. (B) Ursell number versus wave power ratio, P_{ratio} or P_{inner}/P_{outer}. (C) Short-gravity-wave energy flux ratio versus peak direction. (D) Radial histogram of SGW energy flux ratio. Colorbar indicates how observations are sorted by κh. Legend in subplot C shows markers sorted by peak periods, T_p, according to SGW bands in Figs. 3 and 4, and marker size scales according to H_{SGW} values. (For interpretation of the references to colour in this figure legend, the reader is referred to the web version of this article.)

$$S_{ww} = [0.8 + 0.62\log(Ur)]\cos\left[-90° + 90°\tanh\left(\frac{0.73}{Ur}\right)\right], \quad (6)$$

$$A_{ww} = [0.8 + 0.62\log(Ur)]\sin\left[-90° + 90°\tanh\left(\frac{0.73}{Ur}\right)\right], \quad (7)$$

and

$$\beta_{ww} = -90° + 90°\tanh\left(\frac{0.73}{Ur}\right). \quad (8)$$

These nonlinear parameters represent the relative importance of triad interactions in the formation of super-harmonics, which are related to skewed and asymmetric wave orbital velocities (e.g. Hoefel and Elgar, 2003). Table 3 shows values of skewness, asymmetry, and biphase for the maximum value of Ur during each measurement period. These values show that when Ur is ~ 0.1, SGWs remain frequency-dispersive and asymmetry and skewness are negligible.

However, if we assume energetic waves propagating over Shoal E proper (cf. $h \approx 5m$ at the Shoal E ridge in Fig. 1D), then $H_{SGW} \approx 2.5\ m$ and $T_p \approx 10s$ would be related to $Ur \approx 0.6$. This value of Ur results in $S_{ww} = 0.64$, $A_{ww} = -0.17$, and $\beta_{ww} = -15°$. Asymmetry and skewness different from zero produce more energy transfer to super-harmonics (higher breaking tendency) and, in turn, to the LGWs. The ratio of wave height to water depth, however, may indicate that short-wave breaking is not likely to occur, as $H_{SGW}/h \approx 0.5 < 0.78$ (Thornton and Guza, 1982).

During storms when SGW wave heights can attain values ~ 6 m, peak periods reach 12 s and $Ur \approx$ 2.1. Corresponding parameters are expected to be $S_{ww} = 0.4$ $A_{ww} = -0.88$, and $\beta_{ww} = -60°$. During such instances, sea-swell over Shoal E ridge may exhibit a behavior that is relatively more amplitude dispersive than frequency dispersive and short-wave incipient breaking is likely to occur. This breaking could generate additional LGWs energy by the time-varying breakpoint mechanism and might explain larger fluxes at the "outgoing" swale during Falls of 2013 and 2014 (Symonds et al., 1982).

Considering the relation between landward and seaward infragravity energy fluxes, values $R^2 \approx 1$ may indicate negligible dissipation and trapping (as edge waves) between the reflector –the shoreline or the shoal– and the measurement location. Values of R^2 less than 1 indicate seaward fluxes (F^-) were smaller than landward fluxes (F^+), possibly related to the dissipation of seaward LGWs by nearshore

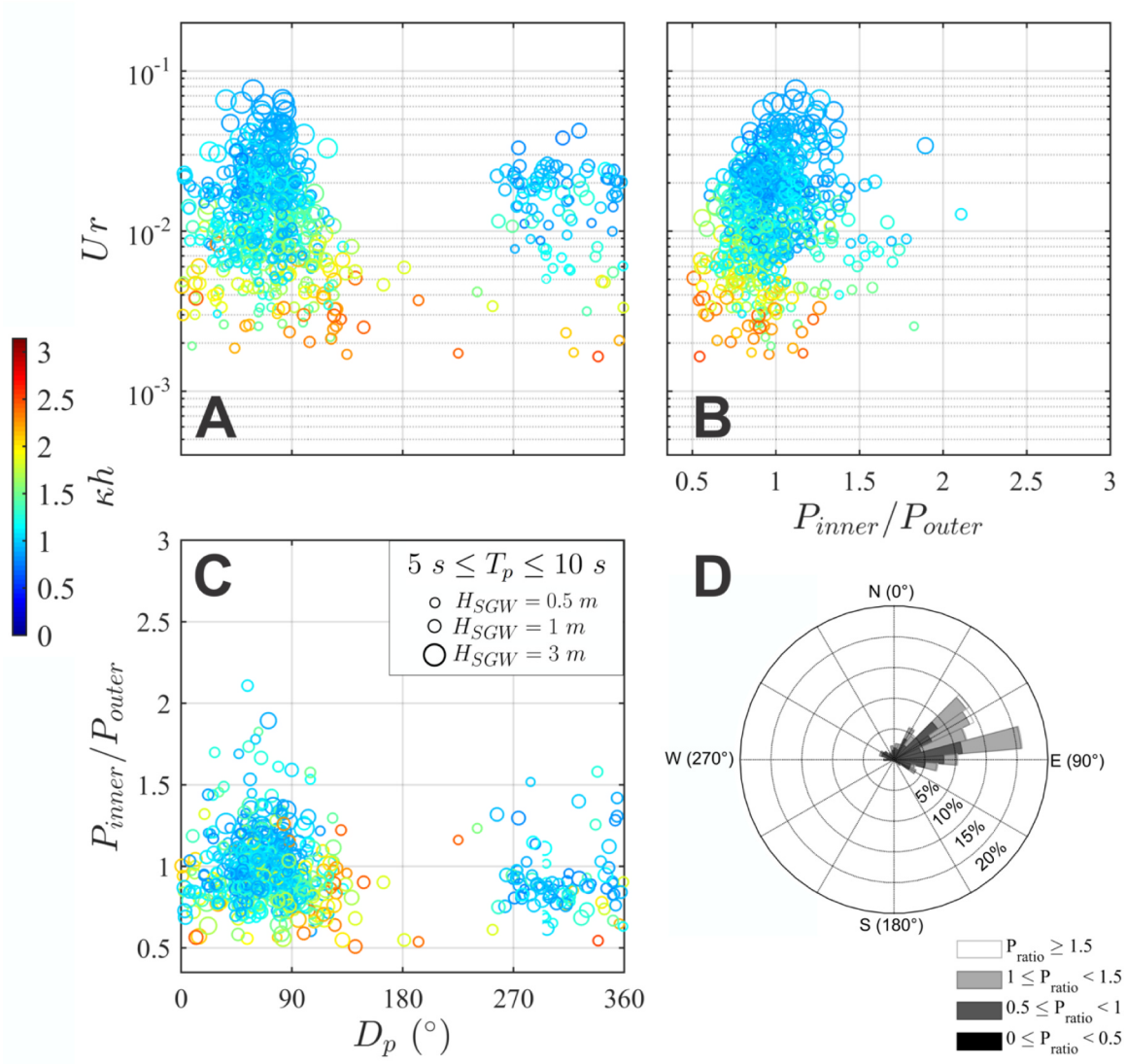

Fig. 6. Ratio of intermediate SGW energy fluxes between swales as a function of short wave properties. The reader is referred to Fig. 5 for plot descriptions.

trapping. Similarly, values of $R^2 > 1$ suggest seaward fluxes were larger than landward fluxes. This situation may be caused by LGW energy produced onshore of Shoal E and radiated seaward that exceeded dissipation and nearshore trapping (Sheremet et al., 2002).

At other sites with gently sloping beaches, R^2 values of ~ 0.5 are found in the shoaling region when onshore LGW energy fluxes increase while variations in offshore fluxes are orders of magnitude smaller (Sheremet et al., 2002). At Cape Canaveral shoals, values $R^2 < 1$ during Fall 2013 suggest the shoaling of short-wave groups close to the breaking location where F^+ is maximum. Values R^2 larger than 1 for directions between 247 °T and 337 °T during Fall 2014 corresponded to $R^2 < 1$ in the landward, cross-shoal direction and suggest, in terms of short-wave shoaling, conditions similar to Fall 2013 experiment.

4.2. Gravity-wave scattering and dissipation over shoal E

4.2.1. Short-gravity-waves

The analysis of sea-swell transformations over shoals should consider, in addition to shoaling and dissipation, the wave field scattering. "Scattering" refers to processes of wave refraction, diffraction, and reflection (Bender and Dean, 2003) that likely exert control on the nearshore wave energy available near capes, and therefore on the long-term maintenance of cuspate forelands (Limber et al., 2017). In the case of SGWs, and without considering diffraction and reflection, differences in P_{ratio} for short and long categories could be explained by the competition between dissipation and refraction. Bottom dissipation, dE/dx, can be assessed by using a relatively simple model of monochromatic waves in horizontal bottoms as (Herbers et al., 2000a, their Eq. 6)

$$\frac{dE}{dx} = -f_w \frac{32\sqrt{2}\pi^2 f^3}{3gc_g \sinh^3(\kappa h)} E^{3/2}, \tag{9}$$

where $f_w = 0.1$ (Herbers et al., 2000a) and $h = 14\ m$. We evaluated four scenarios of extreme short and long SGW dissipation using values found during our observations: small ($E = 0.005\ m^2$) and large waves ($E = 0.7\ m^2$), each case quantified for short ($f = 0.2\ Hz$ and $\kappa = 0.16\ m^{-1}$) and long SGWs ($f = 0.08\ Hz$ and $\kappa = 0.05\ m^{-1}$). Combination of values rendered dE/dx equal to -8.42×10^{-9} (small) and $-1.35 \times 10^{-5}\ m$ (large) for short SGWs, and -8.55×10^{-8} (small) and $-1.37 \times 10^{-4}\ m$ (large) for long SGWs.

Both cases of small short and long SGWs were associated with low dissipation values $O(10^{-8}\ m)$ and probably with a low effect of refraction. These scenarios gave values of $P_{ratio} \approx 1$ corresponding to observations in the low Ur extremes in Fig. 5B, i.e. $Ur \approx 5 \times 10^{-4}$ for red dots and $Ur \approx 4 \times 10^{-3}$ for blue asterisks. On the other hand, the effect of refraction on large waves would drastically differ between short and long SGWs. Calculated dissipation values are $O(10^{-4})$, with refraction probably

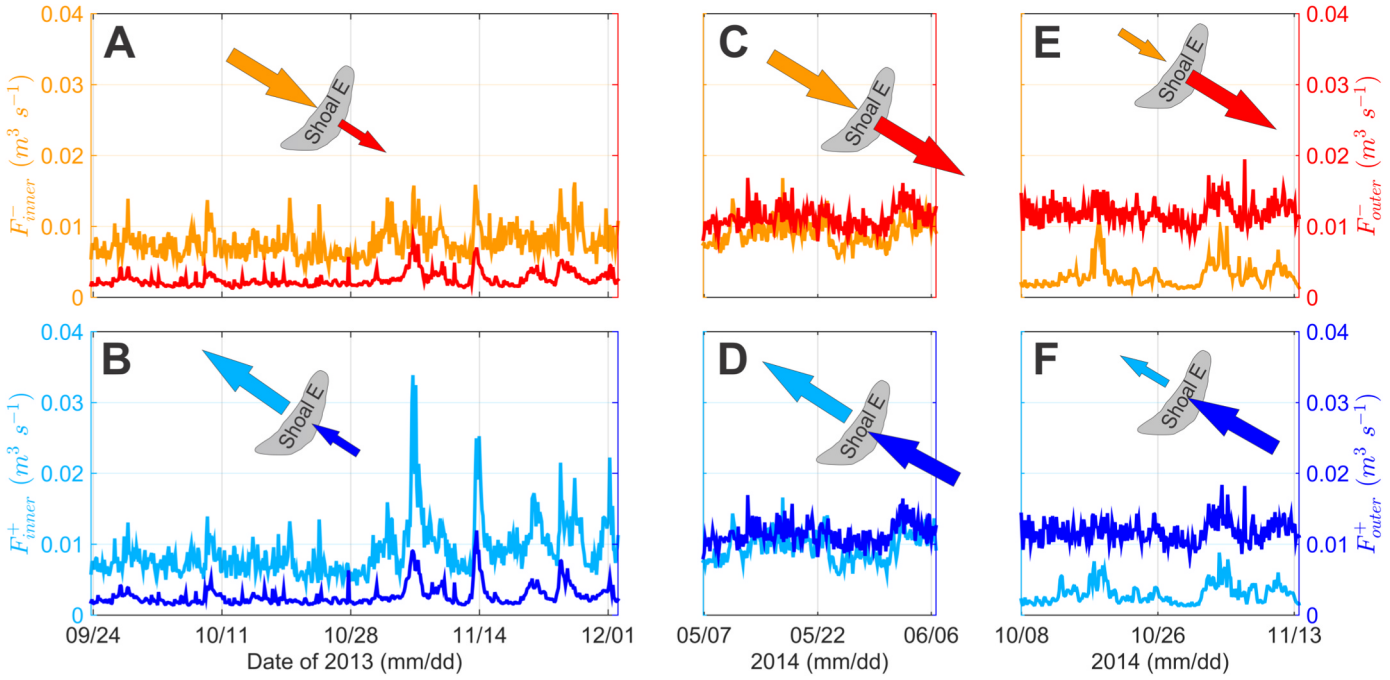

Fig. 7. (A–F) Time series plots of seaward- (F^-) and landward-directed (F^+) cross-shoal LGW energy fluxes for inner (orange and turquoise lines) and outer (red and blue lines) swales. Panels A, C, and E correspond to F^-, whereas B, D, and F show F^+. (For interpretation of the references to colour in this figure legend, the reader is referred to the web version of this article.)

Table 2
Statistical inference of cross-shoal R^2 values at outer (eastern) and inner (western) swales of Shoal E provides evidence that larger reflection coefficients were found at the outer location[(a)]. P-values in brackets indicate lack of statistical significance at the 99% level, but significance at the 95% confidence level. See (Devore and Berk, 2012, their Section 10.1). "N" stands for number of samples and "STD" for standard deviation.

Experiment	Swale	N	Mean	STD	z[(b)]	p-value
Fall 2013	Inner	566	0.90	0.14	8.8	~ 0
	Outer	1,046	0.96	0.12		
Spring 2014	Inner	247	0.96	0.05	7.3	2×10^{-13}
	Outer	247	0.99	0.04		
Fall 2014	Inner	885	1.00	0.31	2.4	(9×10^{-3})[(c)]
	Outer	611	1.02	0.06		

[(a)] At the 99% of statistical confidence with $z_{crit,0.005} = 2.58$.
[(b)] Positive z indicates larger R^2 values at the outer swale.
[(c)] R^2 not different at 99%, but different at 95% of confidence.

affecting long SGWs more prominently. Therefore, short SGWs in the large waves category dissipated ($(P_{ratio} \approx 0.5$ for $Ur \approx 4 \times 10^{-3})$, whereas P_{ratio} for long SGWs in the large waves category ($Ur \approx 1 \times 10^{-1}$) ranged between 0.8 and 1.3 (Fig. 5B). These values suggest that both categories of large SGWs dissipated over Shoal E, but refraction compensated this dissipation and produced, at times, values of P_{ratios} larger than 1. The lack of understanding of specific scattering mechanisms (including diffraction and reflection), which likely would depend upon bottom sedimentary properties, angle of approach, and ambient currents, will be the focus of future studies and probably will explain the scatter and values that fell outside the categories proposed.

4.2.2. Long-gravity-waves

The partial reflection of LGWs by complicated bathymetry has been theorized for several idealized profiles (Liu et al., 2013, and references therein), and has been confirmed at submarine canyons (Thomson et al., 2005, 2007). Over cape-related shoals, LGWs reflection may be analogous to the transmission of a stream of electrons through an attractive, square well potential (Bohm, 1989, Section 11.7 therein) that implies the partition of incoming wave energy into transmitted and partially-reflected energies (Mei et al., 2005, Section 4.4 therein). Recent contributions in this regard include long wave propagation over smooth topography (Liu et al., 2012), infragravity variability linked to sea-swell scattering (Zou, 2011), and coupled-mode solutions of short-wave motions over arbitrary topography and currents (Belibassakis et al., 2011, and others). The coupled-mode solutions may be extended to include LGWs variability and will be considered for future studies.

In two dimensions, and after assuming that the effects of horizontally-sheared currents are not important (e.g., Liu et al., 1990), short-wave-groups scattering over shoals may generate LGWs via three mechanisms: second-order, forced LGWs induced by depth variations; changes in long-wave volume flux; and spatial gradients in stresses related to wave orbital velocities (cf. Zou, 2011, Section 5 therein). These mechanisms depend upon topographic characteristics (water depth, slope, and curvature). Fig. 1D illustrates Shoal E profile asymmetry that is characterized by relatively steeper and negative outer slopes and curvatures, respectively, in contrast to relatively milder and positive inner slopes and curvature.

Shoal E's asymmetric morphology thus likely produce asymmetries in LGW generation and might explain differences in fluxes between swales. The effects of horizontally-sheared tidal and subtidal (wind-driven) flows may also contribute to those inner-outer swale differences in LGW generation, but further analysis would be required to evaluate these ideas (e.g., Liu et al., 1990; Thomson et al., 2005).

4.3. Wave energy flux increase at shoals: potential implications for the long-term maintenance of capes

Our results suggest that Shoal E exerted control on gravity wave variability, at times, by increasing the net energy flux at the "outgoing" swale, i.e. the swale located in the lee of the shoal with respect to the short-wave propagation. The increase of short-gravity-wave energy flux at the lee of isolated, cape-related shoals is expected due to the well-known process of refraction (Munk and Traylor, 1947). The increase of SGW energy flux due to refraction further highlights the potential for harvesting this type of renewable energy offshore of capes.

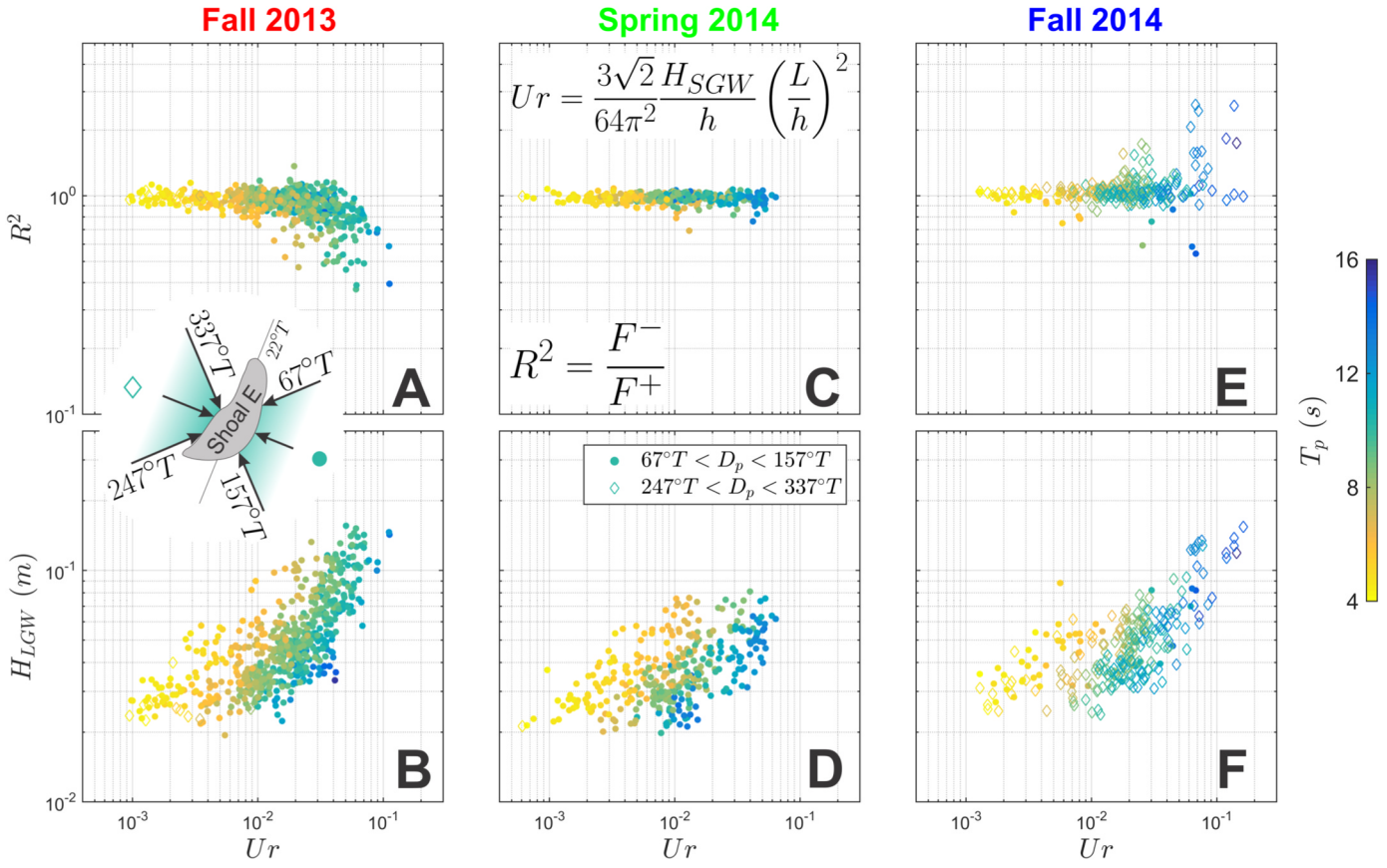

Fig. 8. (A, C, and E) Reflection coefficients, R^2 versus Ursell parameters at the outer swale, Ur sorted by peak periods, T_p, and peak directions, D_p relative to shoal orientation (in $°T$) indicated Shoal E was in the shoaling zone when waves were of greater height and wavelength. Generally, short-waves propagated across Shoal E in the landward direction during Fall 2013 (A and B) and Spring 2014 (C and D), and in the seaward direction during Fall 2014 (E and F). For $Ur > 2 \times 10^{-2}$, $R^2 > 1$ corresponded to $247°T < D_p < 337°T$ (Fall 2014), whilst $R^2 < 1$ occurred when $67°T < D_p < 157°T$ during Fall 2013 and Spring 2014. (B, D, and F) Long gravity significant wave heights, H_{LGW} were proportional to Ur and T_p, and ranged from 2×10^{-2} to 1.5×10^{-1} m.

Table 3
Values of biphase, β_{ww}, skewness, S_{ww}, and asymmetry, A_{ww} correspondent to the maximum values of Ur suggest SGWs behaved as frequency-dispersive waves during all experiments over the swales of Shoal E.

Experiment	max. Ur	S_{ww}	A_{ww}	β_{ww} (°)
Fall 2013	0.12	0.23	-3.7×10^{-6}	-9.4×10^{-4}
Spring 2014	0.07	0.08	-2.3×10^{-10}	-1.6×10^{-7}
Fall 2014	0.25	0.43	-4.0×10^{-3}	-5.2×10^{-1}

We speculate that cape-related shoals initiate the energy transfer from SGWs to LGWs further offshore compared to a typical gently-sloping beach. This LGW forcing implies that short-wave breakers near cuspate coastlines migrate further onshore as the surfzone narrows. Also, free LGWs should be reflected from the cuspate shoreline (Cape Canaveral proper and False Cape) in patterns similar to convex mirrors (Whitham, 1999, Section 7.8 therein) and both incoming and outgoing LGWs would be dissipated by the shore-attached shoal (cf. Fig. 1D).

Over time scales of years to centuries, SGW transformation over shoals is thought to exert control on the maintenance of cuspate forelands. Short-gravity wave refraction may focus the energy at the lee of isolated shoals, which would also force infragravity motions. Wave energy should dissipate over the gentle bottom slope of the shore-attached shoal and may reduce the sediment transport capacity at the cape tip. This energy reduction might enhance gradients in long-shore sediment transport at cuspate shorelines that would translate into lower shoreline migration rates. Lower (refraction induced) rates would provide the anti-diffusional mechanism that is proposed to operate over complex inner-shelf bathymetries in low-angle wave regimes (Limber et al., 2017). Interactions among infragravity, tidal, and subtidal motions (that may modulate LGW variability) thus ought to dominate the cross-shelf water circulation near cuspate forelands.

4.4. Potential trapping of LGWs: methodological limitations

The main limitation in our methods relates to assuming linear wave theory to calculate the SGW energy fluxes, and cross-shoal propagation to apply Eq. (4) for LGW energy fluxes. These assumptions simplify the physics but neglect nonlinear processes and along-shoal motions. This situation, however, may hold only when SGWs propagate in directions close to perpendicular to the Shoal E axis ($67°T < D_p < 157°T$ or $247°T < D_p < 337°T$) .

The sparsity of measurements over the shoals limits the coverage of wave variability. Our analyses did not consider along-shoal changes, likely influenced by trapped edge waves and partial reflections (Eckart, 1951; Huntley et al., 1981; Thomson et al., 2007; Rijnsdorp et al., 2015, and others). Values of $R^2 < 1$ suggest that the dissipation of energy during weakly-nonlinear conditions may be attributed in part to edge waves. In addition, the directional spectra of LGWs (not shown) indicate spreads of up to ~ 90°. These values suggest that errors associated with assuming cross-shoal LGW propagation are not negligible. Future research should focus on analyzing gravity wave dynamics (including 2D LGW propagation) with field data derived from arrays of instruments (e.g., Herbers et al., 1994; Sheremet et al., 2005).

5. Summary and conclusions

We compared short wave energy fluxes between inner (landward) and outer (seaward) swales of Shoal E, along the inner-shelf adjacent to Cape Canaveral, to confirm that isolated, cape-related shoals exert control on wave transformation. Our observations suggest that Shoal E affected large waves (heights larger than 1 m) by dissipating both short and long SGWs, but only refracting long SGWs. Small SGWs (heights smaller than 1 m) appeared to be not affected by Shoal E in terms of energy flux ratios between swales.

Infragravity energy fluxes between swales followed three regimes: larger fluxes at inner swale than outer swale during Fall 2013; same order of magnitude in fluxes at both swales during Spring 2014; and larger fluxes at the outer swale relative to the inner swale during Fall 2014. The opposite tendency observed during Fall seasons was explained by a short-wave seaward propagation during Fall 2014 (in opposition to a landward propagation during Fall 2013).

We speculate that short-wave energy may be transferred to LGWs at isolated and shore-attached shoals, and prevented from reaching the cape and adjacent shorelines. This transformation, along with refraction and dissipation of SGWs should influence the long-term maintenance of cape morphology. The complete spectrum of wave energy, specially the LGW motion structure, was not resolved, and we anticipate that it should include trapped edge waves and partially-reflected motions in different directions. Our findings and limitations highlight the need to further study wave dynamics over cape-related shoals and to better understand their influence on the overall morphodynamics near cuspate forelands.

Acknowledgements

Study collaboration and funding were provided by the U.S. Department of the Interior, Bureau of Ocean Energy Management, Environmental Studies Program, Washington, DC under Agreement Number M13AC00012. Thanks to Viktor Adams, Michael Dickson, Patrick McGovern, Sangdon So, Lauren Ross, Jackie Branyon, Mohammad Al-Khaldi, Ahmad Yousif, Alessandro Lopes Aguiar, Renan Peixoto Rosario, and all that helped with fieldwork for this project. Discussions with Alex Sheremet, Maitane Olabarrieta, and Ismael Marino-Tapia are greatly appreciated. JFPA acknowledges the support from the Fulbright Commission, the U.S. Department of State, the Ministry of Education of Colombia, University of Florida College of Liberal Arts and Sciences and Department of Geological Sciences, and EAFIT University. SMP acknowledges the support of the American Society for Engineering Education/Naval Research Laboratory Postdoctoral Fellow Program. We thank Prof. Charitha Pattiaratchi and an anonymous reviewer for their comments and suggestions on an earlier version of this manuscript.

References

Aagaard, T., Greenwood, B., 2008. Infragravity wave contribution to surf zone sediment transport - the role of advection. Mar. Geol. 251, 1–14.
Alsina, J.M., Padilla, E.M., Cáceres, I., 2016. Sediment transport and beach profile evolution induced by bi-chromatic wave groups with different group periods. Coast. Eng. 114, 325–340.
Ashton, A.D., Murray, A.B., 2006. High-angle wave instability and emergent shoreline shapes: 1. Modeling of sand waves, flying spits, and capes. J. Geophys. Res. 111 (F04011), 1–19.
de Bakker, A.T.M., Tissier, M.F.S., Ruessink, B.G., 2015. Nonlinear infragravity-wave interactions on a gently sloping laboratory beach. J. Phys. Oceanogr. 45, 589–605.
de Bakker, A.T.M., Tissier, M.F.S., Ruessink, B.G., 2016. Beach steepness effects on nonlinear infragravity-wave interactions: a numerical study. J. Geophys. Res. 121, 554–570.
Baldock, T.E., 2006. Long wave generation by the shoaling and breaking of transient wave groups on a beach. Proc. R. Soc. Lond. Ser. A 462, 1853–1876.
Beji, S., Battjes, J.A., 1993. Experimental investigation of wave propagation over a bar. Coast. Eng. 19, 151–162.
Belibassakis, K.A., Gerostathis, T.P., Athanassoulis, G.A., 2011. A coupled-mode model for water wave scattering by horizontal, non-homogeneous current in general bottom topography. Appl. Ocean Res. 33, 384–397.
Bendat, J.S., Piersol, A.G., 2010. Random Data, 4th Edition. Wiley Series in Probability and Statistics. John Wiley & Sons, Inc.,
Bender, C.J., Dean, R.G., 2003. Wave field modification by bathymetric anomalies and resulting shoreline changes: a review with recent results. Coast. Eng. 49, 125–153.
Benoit, M., Frigaard, P., Schäffer, H.A., August 1997. Analysing multidirectional wave spectra: a tentative classification of available methods. In: Proceedings of the Seminar on Multidirectional Waves and their Interaction with Structures.
Berthot, A., Pattiaratchi, C., 2005. Maintenance of headland-associated linear sandbanks: modelling the secondary flows and sediment transport. Ocean Dyn. 55, 526–540.
Bertin, X., de Bakker, A., van Dongeren, A., Coco, G., Andre, G., Ardhuin, F., Bonneton, P., Bouchette, F., Castelle, B., Crawford, W.C., Davidson, M., Deen, M., Dodet, G., Guerin, T., Inch, K., Leckler, F., McCall, R., Muller, H., Olabarrieta, M., Roelvink, D., Ruessink, G., Sous, D., Stutzmann, E., Tissier, M., 2018. Infragravity waves: from driving mechanisms to impacts. Earth-Sci. Rev. 177, 774–799.
Bishop, C.T., Donelan, M.A., 1987. Measuring waves with pressure transducers. Coast. Eng. 11, 309–328.
Bohm, D., 1989. Quantum Theory. Dover Publications, Inc.
Bowen, A.J., Guza, R.T., 1978. Edge waves and surf beat. J. Geophys. Res. 83 (C4), 1913–1920.
Bowers, E.C., 1977. Harbour resonance due to set-down beneath wave groups. J. Fluid Mech. 79, 71–92.
Clark, D.B., Elgar, S., Raubenheimer, B., 2012. Vorticity generation by short-crested wave breaking. Geophys. Res. Lett. 39 (L24604), 1–6.
Coco, G., Burnet, T.K., Werner, B.T., Elgar, S., 2003. Test of self-organization in beach cusp formation. J. Geophys. Res. 108 (C3), 46,1–46,11.
Davidson-Arnott, R., 2010. Introduction to Coastal Processes and Geomorphology. Cambridge University Press.
Devore, J.L., Berk, K.N., 2012. Modern Mathematical Statistics with Applications. Springer Texts in Statistics. Springer Science + Bussiness Media.
Diaz-Hernandez, G., Mendez, F.J., Losada, I.J., Camus, P., Medina, R., 2015. A nearshore long-term infragravity wave analysis for open harbours. Coast. Eng. 97, 78–90.
Doering, J.C., Bowen, A.J., 1995. Parametrization of orbital velocity asymmetries of shoaling and breaking waves using bispectral analysis. Coast. Eng. 26, 15–33.
Doering, J.C., Bowen, A.J., 1986. Shoaling surface gravity waves: A bispectral analysis. In: Proceedings of the 20th International Conference in Coastal Engineering. pp. 150–162.
Eckart, C., 1951. Surface waves on water of variable depth. Lecture notes, fall semester, 1950–51, Scripps Institution of Oceanography, University of California.
Elgar, S., Guza, R.T., 1985. Observations of bispectra of shoaling surface gravity waves. J. Fluid Mech. 161, 425–448.
Elgar, S., Herbers, T.H.C., Okihiro, M., Oltman-Shay, J., Guza, R.T., 1992. Observations of infragravity waves. J. Geophys. Res. 97 (C10), 15,573–15,577.
Elgar, S., Guza, R.T., Freilich, M.H., 1993. Observations of nonlinear interactions in directionally spread shoaling surface gravity waves. J. Geophys. Res. 98, 20,299–20,305.
Elgar, S., Raubenheimer, B., Guza, R.T., 2005. Quality control of acoustic doppler velocimeter data in the surfzone. Meas. Sci. Technol. 16, 1889–1893.
Feddersen, F., 2014. The generation of surfzone eddies in a strong alongshore current. J. Phys. Oceanogr. 44, 600–617.
Field, M.E., Duane, D.B., March 1974. Geomorphology and sediments of the inner continental shelf, cape canaveral, florida. Technical Memorandum 42, United States Army Corps of Engineers Coastal Engineering Center, Kingman Building, Fort Belvoir, VA 22060, USA.
Filipot, J.-F., Ardhuin, F., Babanin, A.V., 2010. A unified deep-to-shallow water wave-breaking probability parameterization. J. Geophys. Res. 115 (C04022), 1–15.
Geyer, W.R., 1993. Three-dimensional tidal flow around headlands. J. Geophys. Res. 98, 955–966.
Goring, D.G., Nikora, V.I., 2002. Despiking acoustic doppler velocimeter data. J. Hydraul. Eng. 128 (1), 117–126.
Guo, J., 2002. Simple and explicit solution of wave dispersion equation. Coast. Eng. 45, 71–74.
Guza, R.T., Thornton, E.B., 1982. Swash oscillations on a natural beach. J. Geophys. Res. 87 (C1), 483–491.
Hasselmann, K., 1962. On the non-linear energy transfer in a gravity-wave spectrum. part 1. general theory. J. Fluid Mech. 12, 481–500.
Herbers, T.H.C., Elgar, S., Guza, R.T., 1994. Infragravity-frequency (0.005–0.05 hz) motions on the shelf. Part I: forced waves. J. Phys. Oceanogr. 24, 917–927.
Herbers, T.H.C., Elgar, S., Guza, R.T., O'Reilly, W.C., 1995. Infragravity-frequency (0.005–0.05 Hz) motions on the shelf. Part II: free waves. J. Phys. Oceanogr. 25, 1063–1079.
Herbers, T.H.C., Hendrickson, E.J., O'Reilly, W.C., 2000a. Propagation of swell across a wide continental shelf. J. Geophys. Res. 105, 19729–19737.
Herbers, T.H.C., Russnogle, N.R., Elgar, S., 2000b. Spectral energy balance of breaking waves within the surf zone. J. Phys. Oceanogr. 30, 2723–2737.
Hoefel, F., Elgar, S., 2003. Wave-induced sediment transport and sandbar migration. Science 299, 1885–1887.
Holthuijsen, L.H., 2007. Waves in Oceanic and Coastal Waters. Cambridge University Press.
Huntley, D.A., Guza, R.T., Thornton, E.B., 1981. Field observations of surf beat, 1. progressive edge waves. J. Geophys. Res. 1986, 6451–6466.
Janssen, T.T., Herbers, T.H.C., Battjes, J.A., 2006. Generalized evolution equations for nonlinear surface gravity waves over two-dimensional topography. J. Fluid Mech. 552, 393–418.
Kaergaard, K., Fredsoe, J., 2013. A numerical shoreline model for shorelines with large curvature. Coast. Eng. 74, 19–32.

Kirby, J.T., Dalrymple, R.A., 1983. A parabolic equation for the combined refraction-diffraction of stokes waves by mildly varying topography. J. Fluid Mech. 136, 453–466.
Kline, S.W., 2013. Influence of Wave Energy Dissipation on the Geomorphic Behavior of Rocky and Sandy Coasts (Ph.D. Thesis). University of Florida.
Kumar, N., Voulgaris, G., List, J.H., Warner, J.C., 2013. Alongshore momentum balance analysis on a cuspate foreland. J. Geophys. Res. 118, 5280–5295.
Lamas, L., Peliz, A., Dias, J., Oliveira, P.B., Angelico, M.M., Castro, J.J., Fernandes, J.N., Trindade, A., Cruz, T., 2017. Diurnal variability of inner-shelf circulation in the lee of a cape under upwelling conditions. Cont. Shelf Res. 143, 67–77.
Lentz, S.J., Fewings, M.R., 2012. The wind- and wave-driven inner-shelf circulation. Annu. Rev. Mar. Sci. 4, 317–343.
Limber, P.W., Adams, P.P.N., Murray, A.B., 2017. Modeling large-scale shoreline change caused by complex bathymetry in low-angle wave climates. Mar. Geol. 383, 55–64.
Liu, H.-W., Yang, J., Lin, P., 2012. An analytic solution to the modified mild-slope equation for wave propagation over one-dimensional piecewise smooth topographies. Wave Motion 49, 445–460.
Liu, H.-W., Luo, J.-X., Lin, P., Liu, R., 2013. Analytical solution for long-wave reflection by a general breakwater or trench with curvilinear slopes. J. Eng. Mech. 139, 229–245.
Liu, P.L.-F., 1989. A note on long waves induced by short-wave groups over a shelf. J. Fluid Mech. 205, 163–170.
Liu, P.L.-F., Dingemans, M.W., Kostense, J.K., 1990. Long-wave generation due to the refraction of short-wave groups over a shear current. J. Phys. Oceanogr. 20, 53–59.
Longuet-Higgins, M.S., Stewart, R.W., 1964. Radiation stresses in water waves; a physical discussion, with applications. Deep-Sea Res. 11, 529–562.
McNinch, J.E., Luettich Jr, R.A., 2000. Physical processes around a cuspate foreland: implications to the evolution and long-term maintenance of a cape-associated shoal. Cont. Shelf Res. 20.
Mei, C.C., Benmoussa, C., 1984. Long waves induced by short-wave groups over an uneven bottom. J. Fluid Mech. 139, 219–235.
Mei, C.C., Stiassnie, M., Yue, D. K.-P., 2005. Theory and Applications of Ocean Surface Waves. Part 1: Linear Aspects. Vol. 23 of Advanced Series in Ocean Engineering. World Scientific.
Munk, W.H., 1949. Surf beats. EOS Trans. Am. Geophys. Union (EOS) 30 (6), 849–854.
Munk, W.H., Traylor, M.A., 1947. Refraction of ocean waves: a process linking underwater topography to beach erosion. J. Geol. 55, 1.
Murray, A.B., Ashton, A.D., 2013. Instability and finite-amplitude self-organization of large-scale coastline shapes. Philos. Trans. R. Soc. Lond. Ser. A 371, 1–15.
Okihiro, M., Guza, R.T., 1995. Infragravity energy modulation by tides. J. Geophys. Res. 100 (C8), 16,143–16,148.
Okihiro, M., Guza, R.T., Seymour, R.J., 1992. Bound infragravity waves. J. Geophys. Res. 97 (C7), 11,453–11,469.
Olsen Associates, I., August 2013. Brevard county, florida, federal shore protection project, south reach, 2010 project renourishment, 3-year post-construction monitoring of the canaveral shoals ii offshore borrow area (june 2013). Tech. rep., Olsen Associates, Inc., 2618 Herschel Street, Jacksonville, FL 32204.
Paniagua-Arroyave, J.F., Adams, P.N., Valle-Levinson, A., Parra, S.M., 2018. Infragravity wave heights and ambient motions at cape canaveral shoals. Data Set., Mendeley Data.
Pomeroy, A., Lowe, R., Symonds, G., van Dongeren, A., Moore, C., 2012. The dynamics of infragravity wave transformation over a fringing reef. J. Geophys. Res. 117 (C11022), 1–17.
Raubenheimer, B., Elgar, S., Guza, R.T., 1998. Estimating wave heights from pressure measured in sand bed. J. Waterw. Port. Coast. Ocean Eng. 124 (3), 151–154.
RDI, January 2011. Acoustic doppler current profiler principles of operation a practical primer. Tech. rep., Teledyne RD Instruments.
Rijnsdorp, D.P., Ruessink, G., Zijlema, M., 2015. Infragravity-wave dynamics in a barred coastal region, a numerical study. J. Geophys. Res. 120, 1–22.
Rodriguez, A., Sanchez-Arcilla, A., Redondo, J.M., Bahia, E., Sierra, J.P., 1995. Pollutant dispersion in the nearshore region: modelling and measurements. Water Sci. Technol. 32 (9–10), 169–178.
Roelvink, D., Reniers, A., van Dongeren, A., van Thiel de Vries, J., McCall, R., Lescinski, J., 2009. Modelling storm impacts on beaches, dunes and barrier islands. Coast. Eng. 56, 1133–1152.
Ruessink, B.G., 1998. Bound and free infragravity waves in the nearshore zone under breaking and nonbreaking conditions. J. Geophys. Res. 103 (C6), 12,795–12,805.
Schäffer, H.A., 1993. Infragravity waves induced by short-wave groups. J. Fluid Mech. 247, 551–588.
Schratzberger, M., Larcombe, P., 2014. The role of the sedimentary regime in shaping the distribution of subtidal sandbank environments and the associated meiofaunal nematode communities: an example from the southern north sea. PLoS One 9 (10 e109445), 1–21.
Sheremet, A., Guza, R.T., Elgar, S., Herbers, T.H.C., 2002. Observations of nearshore infragravity waves: seaward and shoreward propagating components. J. Geophys. Res. 107 (C8), 1–10.
Sheremet, A., Guza, R.T., Herbers, T.H.C., 2005. A new estimator for directional properties of nearshore waves. J. Geophys. Res. 110, 1–11.
Signell, R.P., Geyer, W.R., 1990. Transient eddy formation around headlands. J. Geophys. Res. 96 (C2), 2561–2575.
Symonds, G., Huntley, D.A., Bowen, A.J., 1982. Two-dimensional surf beat: long wave generation by a time-varying breakpoint. J. Geophys. Res. 87 (C1), 492–498.
Thieler, E.R., Foster, D.S., Himmelstoss, E.A., Mallinson, D.J., 2014. Geologic framework of the northern north carolina, USA inner continental shelf and its influence on coastal evolution. Mar. Geol. 348, 113–130.
Thompson, D.M., Plant, N.G., Hansen, M.E., 2015. Analysis of bathymetric surveys to identify coastal vulnerabilities at cape canaveral, Florida. Open File Report 2015–1180, U.S. Geological Survey.
Thomson, J., Elgar, S., Herbers, T.H.C., 2005. Reflection and tunneling of ocean waves observed at a submarine canyon. Geophys. Res. Lett. 32 (L10602), 1–4.
Thomson, J., Elgar, S., Raubenheimer, B., Herbers, T.H.C., Guza, R.T., 2006. Tidal modulation of infragravity waves via nonlinear energy losses in the surfzone. Geophys. Res. Lett. 33 (L05601).
Thomson, J., Elgar, S., Herbers, T.H.C., Raubenheimer, B., Guza, R.T., 2007. Refraction and reflection of infragravity waves near submarine canyons. J. Geophys. Res. 112, 1–9.
Thomson, R.E., Emery, W.J., 2014. Data Analysis Methods in Physical Oceanography. Elsevier B.V.
Thornton, E.B., Guza, R.T., 1982. Energy saturation and phase speeds measured on a natural beach. J. Geophys. Res. 87, 9499–9505.
Torres-Freyermuth, A., Hsu, T.-J., 2014. On the mechanisms of low-frequency wave attenuation by muddy seabeds. Geophys. Res. Lett. 41, 2870–2875.
Tucker, M.J., 1950. Surf beats: sea waves of 1–5 min period. Proc. R. Soc. Lond. Ser. A 202, 565–573.
Ursell, F., 1953. The long-wave paradox in the theory of gravity waves. Math. Proc. Camb. Philos. Soc. 49, 685–694.
Whitham, G.B., 1999. Linear and Nonlinear Waves. John Wiley & Sons, Inc.
Yoo, D., O'Connor, B.A., 1988. Diffraction of waves in caustics. J. Waterw. Port., Coast., Ocean Eng. 114, 715–731.
Young, A.P., Guza, R.T., Adams, P.N., O'Reilly, W.C., Flick, R.E., 2012. Cross-shore decay of cliff top ground motions driven by local ocean swell and infragravity waves. J. Geophys. Res. 117 (C06029), 1–12.
Young, I.R., Eldeberky, Y., 1998. Observations of triad coupling of finite depth wind waves. Coast. Eng. 33, 137–154.
Zou, Q., 2011. Generation, transformation, and scattering of long waves induced by a short-wave group over finite topography. J. Phys. Oceanogr. 41, 1842–1859.